



Divergent iron dissolution pathways controlled by sulfuric and nitric acids from the ground-level to the upper mixing layer

Guochen Wang¹, Xuedong Cui², Bingye Xu³, Can Wu⁴, Minkang Zhi¹, Keliang Li¹, Liang Xu⁵, Qi Yuan⁶, Yuntao Wang⁷, Yele Sun⁸, Zongbo Shi⁹, Akinori Ito¹⁰, Shixian Zhai¹¹, Weijun Li^{1,8*}

- ¹State Key Laboratory of Ocean Sensing and Department of Atmospheric Sciences, School of Earth Sciences, Zhejiang University, Hangzhou 310027, China
 - ²Hangzhou Meteorological Bureau, Hangzhou 310051, China
 - ³Ecological and Environmental Monitoring Center of Zhejiang Province, Hangzhou 310007, China
 - ⁴Key Lab of Geographic Information Science of the Ministry of Education, School of Geographic Sciences,
- 10 East China Normal University, Shanghai 210062, China
 - ⁵College of Sciences, China Jiliang University, Hangzhou 310018, China
 - ⁶College of Environmental Science and Engineering, Ocean University of China, Qingdao 266100, China
 - ⁷State Key Laboratory of Satellite Ocean Environment Dynamics, Second Institute of Oceanography, Ministry of Natural Resources, Hangzhou 310012, China
- ⁸State Key Laboratory of Atmospheric Boundary Layer Physics and Atmospheric Chemistry, Institute of Atmospheric Physics, Chinese Academy of Sciences, Beijing 100029, China
 - ⁹School of Geography, Earth and Environmental Sciences, University of Birmingham, Birmingham B17 8PS, UK
 - ¹⁰Yokohama Institute for Earth Sciences, Japan Agency for Marine-Earth Science and Technology (JAMSTEC), Yokohama, Kanagawa 236-0001, Japan
- 20 ¹¹Earth and Environmental Sciences Programme and Graduation Division of Earth and Atmospheric Sciences, Faculty of Science, The Chinese University of Hong Kong, Sha Tin, Hong Kong SAR, China

Correspondence to: Weijun Li (liweijun@zju.edu.cn)

Abstract. Iron (Fe) plays a crucial role in the global biogeochemical cycle, marine ecosystems, and human health. Despite extensive research on Fe dissolution, the understanding of the mechanism of the Fe acidification process remains highly controversial. Here, we revealed significant differences in Fe acid dissolution between the upper mixing layer and the ground-level of a megacity. The results showed that air masses with elevated $n[SO_4^{2-}]/n[NO_3^{-}]$ ratios (5.4 ± 3.7) yielded more enhanced iron solubility (%Fe_S, 8.7 ± 2.4%) in the upper mixing layer after atmospheric aging compared to those (1.6 \pm 0.7 and 3.3 \pm 0.4%, respectively) at the ground-level near source regions of acidic gases. Further analysis suggested that Fe dissolution is primarily driven by sulfuric acid in the upper mixing layer different from nitric acid at the ground-level, attributing to the aging processes of acidic species during long-range transport. %Fe_S also exhibits a clear size dependence: sulfuric-acid dominates in submicron aerosols ($D_p < 1 \mu m$), leading to elevated %Fe_S(3.4 \pm 3.8%), whereas alkaline mineral dust in supermicron particles ($D_p > 1 \mu m$) neutralizes nitric acid and suppresses Fe dissolution (1.7 \pm 2.2%). This finding highlighted that sulfuric acid dominates Fe acidification process in the upper layer and fine particles, but the contribution of nitric acid to Fe dissolution at the ground-level is equally important. Our study provides new data sets for testing atmospheric model's capability to simulate dissolved Fe concentration and deposition and will help to improve the accuracy of Fe solubility predictions.





1 Introduction

40

45

55

60

Iron (Fe) is an ubiquitous but essential element for life and plays a crucial role in the global biogeochemical cycle, marine ecosystems, and human health (Mahowald et al., 2009; Martin, 1990; Boyd and Ellwood, 2010). Despite its abundance in the earth's crust, Fe is often a growth limiting factor, controlling primary productivity in up to one-third of the world's oceans with high nutrient low chlorophyll (HNLC), thereby influencing carbon sequestration (Mahowald et al., 2009; Martin, 1990). Additionally, redox cycling of Fe affects the formation of reactive oxygen species (ROS) in aqueous reactions, causing adverse health effects (Vidrio et al., 2008; Chen et al., 2024a). The vital role of Fe in global climate change and human health underscores the need to understand the mobilization and dissolution of Fe during atmospheric transformations (Jickells et al., 2005; Martínez-García et al., 2014; Boyd et al., 2007; Fang et al., 2017).

The acidification process of insoluble Fe-containing aerosols by acids (e.g., H₂SO₄ and HNO₃) has been identified as the controlling factor in Fe solubility (%Fe₈) in particles (Baker et al., 2021; Ingall et al., 2018; Longo et al., 2016; Meskhidze, 2005; Shi et al., 2015). In this process, acids condense on the surface of insoluble Fe-containing particles and elevate the aerosol acidity. Both laboratory studies (Cwiertny et al., 2008; Shi et al., 2015; Ito and Shi, 2016) and field observations (Lei et al., 2023; Oakes et al., 2010) have shown that the heterogeneous reaction of SO₂ on the surface of mineral dust forms an extremely acidic environment that promotes Fe dissolution. Zhuang et al. (1992) initially proposed the hypothesis of the coupling and feedback mechanism between Fe and sulfur during the long-range transport of Asian dust, underscoring the crucial role of sulfuric acid in dissolving Fe. Similar findings have been documented during the transport of North Africa dust to the Atlantic Ocean (Zhu et al., 1997), in the North India Ocean (Bay of Bengal) (Srinivas et al., 2011), in major U.S. cities like Atlanta (Wong et al., 2020; Oakes et al., 2012), in offshore regions of China (such as the Yellow Sea) (Li et al., 2017; Meskhidze, 2003) and its cities (Zhu et al., 2020), and even within simulated cloud processes (Wang et al., 2019; Chen et al., 2012). However, other studies also indicated that nitric acid can equally or more effectively promote Fe dissolution than sulfuric acid (Zhu et al., 1997; Sakata et al., 2023; Rubasinghege et al., 2010). For instance, recent work by Zhu et al. (2020) determined that nitric acid elevates %Fe_S in urban environments in eastern China, emphasizing its contribution to Fe acid dissolution.

Despite extensive previous research on Fe dissolution, understanding the role of proton-promoted process remains highly controversial. Atmospheric acidification accelerates Fe dissolution, primarily depending on the type and relative abundance of acids and their aging process. Variations in emissions of acidic gases such as SO₂ and NO_x (=NO+NO₂) will consequently affect the formation of H₂SO₄ and HNO₃, creating an acidic environment (Rubasinghege et al., 2010; Ooki and Uematsu, 2005). Moreover, the aging process of acidic species modulates atmospheric chemistry (e.g., aerosol acidity) during long-range transport, thereby influencing Fe dissolution process (Baker et al., 2021; Li et al., 2017; Xu et al., 2023). To estimate proton levels, the atmospheric chemistry models consider thermodynamic processes involving the sulfuric acid and nitric acid systems (Ito, 2011; Myriokefalitakis et al., 2022). However, when the climate models simplify the proton-promoted dissolution scheme, proton concentrations are calculated solely from the ratios of sulfate to calcite (Hamilton et al., 2019).





This simplification cannot truly reflect proton levels and Fe dissolution rate under the regime shift from sulfuric acid to nitric acid (Ito and Xu, 2014). The accuracy of Fe simulation needs to be further verified. Under sustainable reductions of SO₂ emissions, NO_x has replaced SO₂ as the predominant inorganic acid source at the ground-level in most parts of China in the past ten years (Van Der A et al., 2017; Zheng et al., 2018; Geng et al., 2024). Here, we raise the issue of whether the key chemical processes that dominate Fe dissolution differ between the near-surface and the upper mixing layer. However, current field observation has not well documented how Fe dissolution may change with varied heights in eastern China.

To answer this question, we designed field observations in the upper layer of a mountain (Damingshan, DMS) and at the ground-level in a megacity (Hangzhou) to clarify how inorganic acids and their atmospheric aging influence Fe dissolution. By distinguishing air masses arriving at the two altitudes and examining their respective $n[SO_4^{2-}]/n[NO_3^{-}]$ ratios, we systematically compared the acid aging processes and associated Fe acidification under these contrasting atmospheric environments. Our results reveal distinct %Fe_S levels between the upper layer and ground-level, driven by differing acid-processing pathways: sulfuric acid-dominated aging in the upper layer (due to longer distance transport) versus nitric acid-dominated processing at the ground-level.

2 Data and methods

2.1 Sample collection

85

95

100

The field campaigns were conducted during the summer of 2021 in a mountain site (DMS, 30.03°N, 119.00°E, 1483 m) and in the megacity of Hangzhou (HZ, 30.30°N, 120.09°E, 6 m) (Figure S1). The mountain serves as a background environment and is sensitive to the transport of air pollutants from outside. Its high altitude makes it an ideal location for assessing the impacts of anthropogenic emissions in the upper layer. Since mixed-layer height (MLH) data were not available at DMS during the sampling period, we referenced MLH observations from Hangzhou. The results show that the MLH in Hangzhou remained below ~1500 m for most of the time (~92%; Figure S2, unpublished data). Given the relatively short distance between the two sites (~110 km), the MLH in Hangzhou is considered a reasonable proxy for that at DMS. Therefore, owing to its elevation (~1500 m), the mountain site can be considered representative of the upper mixing layer. The urban site in Hangzhou, with a population of 12.52 million by the end of 2023 (Hangzhou Municipal Government, 2024), is one of the densely populated regions in the Yangtze River Delta (YRD).

Sampling was conducted from July 17 to August 19, 2021 for DMS and from September 11 to 21, 2021 for HZ. A medium-flow total suspended particle (TSP) sampler (TH-16A, Wuhan Tianhong Instrument Co., Ltd, China) with a sampling flow rate of 100 L min⁻¹ was deployed to collect aerosol particles on quartz filters. Prior to sampling, the filters were pre-combusted at 600 °C for 6 h to eliminate potential organic contamination. All samples were stored at –20 °C until further analysis. Ascribed to the rainy season in summer (June-October), the sampling was temporarily stopped due to rain events. Totally, seven samples were obtained from mountain site and seven samples were collected from Hangzhou city. Detailed sampling information is presented in Table S1 in the Supplement. A ten-stage cascade impactor (MOUDI 120R,



105

120

125

130



MSP corporation, USA), operating at a flow rate of 30 L min⁻¹, was employed to collect size-resolved aerosol samples with cut points of 18, 10, 5.6, 3.2, 1.8, 1.0, 0.56, 0.32, 0.18, 0.10, and 0.056 μm. Three sets of samples were collected in DMS during the periods of July 29 to August 2, August 8-9, and August 18-19, 2021. Due to the maintenance of instrument, however, no MOUDI samples were collected in HZ. All instruments were installed on open ground in front of the monitoring site.

2.2 Water-soluble inorganic ions

The water-soluble inorganic ions (WSIIs), including $SO_4^{2^-}$, NO_3^- , CI^- , Na^+ , NH_4^+ , K^+ , Mg^{2^+} and Ca^{2^+} in TSP and sizeresolved aerosols (MOUDI) were analyzed with an ion chromatography (DIONEX ICS-600). The detection limits of the measured $SO_4^{2^-}$, NO_3^- , CI^- , Na^+ , NH_4^+ , K^+ , Mg^{2^+} and Ca^{2^+} are 0.021, 0.008, 0.010, 0.018, 0.006, 0.006, 0.009 and 0.022 μg mL⁻¹, respectively. More information about the laboratory chemical analyses can be found in our previous studies (Liu et al., 2022a; Zhu et al., 2020). To distinguish the contribution of anthropogenic emissions to sulfate, sulfate associated with sea salt was subtracted from the measured sulfate in this study. The mass concentration of the non-sea salt sulfate (nss- $SO_4^{2^-}$) can be estimated as follows:

nss-
$$SO_4^{2-} = SO_4^{2-} - 0.25 \times Na^+$$
 (1)

where $SO_4^{2^-}$ and Na^+ are the mass concentrations of $SO_4^{2^-}$ and Na^+ , respectively. 0.25 is the mass ratio of $SO_4^{2^-}$ to Na^+ in pure seawater (Kunwar and Kawamura, 2014). Therefore, the sulfate used in the analysis is $nss-SO_4^{2^-}$.

2.3 Measurements of total and dissolved Fe

The total iron (Fe_T) in TSP and size-resolved aerosols were measured non-destructively using an energy dispersive X-ray fluorescence (ED-XRF) spectrometer (Epsilon 4, PANalytical, Netherlands). A standard reference material (SRM 2786, National Institute of Standards and Technology (NIST), USA) was used to calibrate the instrument before sampling analysis. The measured Fe concentrations were within the NIST certified values, with relative errors between measured and standard values below 10 %. Soluble iron (Fe_S) in the samples was measured using the ferrozine technique following the procedures of Zhu et al. (2022) and Zhi et al. (2025). Briefly, (1) two circular sections (radius = 8 mm) were cut and placed in polypropylene bottles with 20 mL of ammonium acetate solution (0.5 mM, pH ~4.3); (2) after 60 min of sonication, the extracts were filtered through a 0.22 μm PTFE syringe filter; (3) the pH of the solution was adjusted to ~1.0 using 150 μL of concentrated HCl and stored at 4 °C before further analysis; (4) starting to measure the solution, a 0.01 M ascorbic acid was added to the solution and held for 30 minutes to ensure the complete reduction of Fe(III) to Fe(II); (5) adding 0.01M ferrozine solution; (6) adjusted the solution to ~pH 9.5 using ammonium acetate buffer. The absorbance of the solution was measured at 562 nm (max light absorption) and 700 nm (background) (Oakes et al., 2012) by using an UV-Visible spectrophotometer (UV-Vis, Specord 50 Plus, Analytik Jena Instruments, Germany). Ultra-grade ammonium Fe(II) sulfate



135

140

145

155

160



hexahydrate (Sigma-Aldrich, St. Louis, USA) was used for Fe(II) standards. The concentration of Fe(II) obtained from the standard curve was the concentration of dissolved Fe.

The quality assurance/quality control (QA/QC) procedures for soluble Fe measurement included the following steps: (1) the spectrophotometer was powered on and stabilized for 6–8 hours prior to use; (2) the instrument was calibrated using seven ammonium Fe(II) sulfate standards with concentrations of 5, 10, 20, 40, 60, 80, and 100 ng mL⁻¹. The absorbance of each standard was measured at 562 nm (I_{562}) and 700 nm (I_{700}), and the absorbance difference ($\Delta I = I_{562} - I_{700}$) was correlated with Fe(II) concentration. When the coefficient of determination (R²) exceeded 0.995, the instrument was considered properly calibrated; (3) prior to sample analysis, a 0.1 mol L⁻¹ HCl solution (pH = 1) was used as the reference; once the absorbance was displayed nearly to zero, the samples could be measured. (4) the soluble Fe detection limit (0.11 ng m⁻³) was determined as three times the standard deviation of filter blank values (n = 9); (5) blank samples were analyzed in the same way as field samples. All samples were corrected by subtracting the filter blank values. In this study, the calibration yielded an R² of 0.9992 and the absorbance of reference solution displayed zero, indicating excellent instrumental stability and measurement reliability. Iron solubility was calculated using the following equation:

%Fe_S (%) =
$$\frac{\text{Fe}_S}{\text{Fe}_T} \times 100\%$$
 (2)

where Fe_S and Fe_T are the soluble Fe and total Fe, respectively.

2.4 Aerosol pH estimation

The ISORROPIA II thermodynamic equilibrium model (https://www.epfl.ch/labs/lapi/models-and-software/isorropia/) was applied to simulate aerosol pH and liquid waters in size-resolved aerosols by using inorganic chemical species (SO₄²⁻, NO₃⁻, NH₄⁺, Cl⁻, Na⁺, K⁺, Mg²⁺, Ca²⁺), ammonia (NH₃), and meteorological factors (temperature and RH) (Fountoukis and Nenes, 2007), and it was calculated by following equation:

$$pH = -\log_{10}\left(\frac{1000 \times [H_{air}^{+}]}{ALW}\right) \qquad (3)$$

where [H_{air}] is the H⁺ per volume of air (μg m⁻³), ALW is the aerosol liquid water (μg m⁻³). Here, only aerosol water associated with inorganic species is considered, as previous studies have shown that organics contribute only a small fraction (~10%) to the total ALW (Bougiatioti et al., 2016; Wang et al., 2022). [H_{air}⁺] and ALW can be derived directly from the model results. Due to the lack of concurrent ammonia (NH₃) observations during the study period, we used NH₃ (Model G2103, Picarro Inc., USA) from the summer of 2025 (13-26, July) to approximate the ammonia concentration levels in the mountain site (DMS). Although using data from a different period may introduce some uncertainty, this approximation is considered reasonable because the mountain is a high-altitude site (1500 m) with no significant local anthropogenic emission sources, and regional NH₃ mainly originates from natural releases. Under similar seasonal conditions, variations in local NH₃ concentrations are expected to be minor.





3 Results

165

170

175

3.1 Comparison of chemical composition and Fe solubility

Figure 1a shows the time series of TSP mass concentrations at DMS and in HZ during the sampling period. The mean concentrations of aerosol particles reached $41 \pm 17~\mu g~m^{-3}$ at DMS and $86 \pm 28~\mu g~m^{-3}$ in HZ, respectively. The loading of TSP in the upper mixing layer (DMS) was much lower than that at the ground-level (HZ), indicating relatively clean conditions. The pie charts in Figure 1b show that sulfate accounted for 52% in the total measured inorganic ions at DMS, compared to 32% in HZ. In comparison, nitrate accounted for 33% of the measured inorganic ions in HZ, which is more than twice the fraction of nitrate (15%) in the upper mixing layer. Moreover, the average proportion of nitrate in HZ slightly higher than that of sulfate in the total measured inorganic ions during the sampling period, unlike at DMS, where sulfate accounted for a significantly higher proportion than nitrate (Figure 1b). Figure 1c shows the mean concentrations of Fe_T and Fe_S at DMS were 292.3 \pm 86.4 ng m⁻³ and 25.6 \pm 11.5 ng m⁻³, respectively, which were significantly lower than those of 2094.9 \pm 637.0 ng m⁻³ and 69.9 \pm 24.8 ng m⁻³ in HZ. However, the %Fe_S at DMS was 8.7 \pm 2.4%, 2-3 times higher than that of 3.3 \pm 0.4% in HZ.

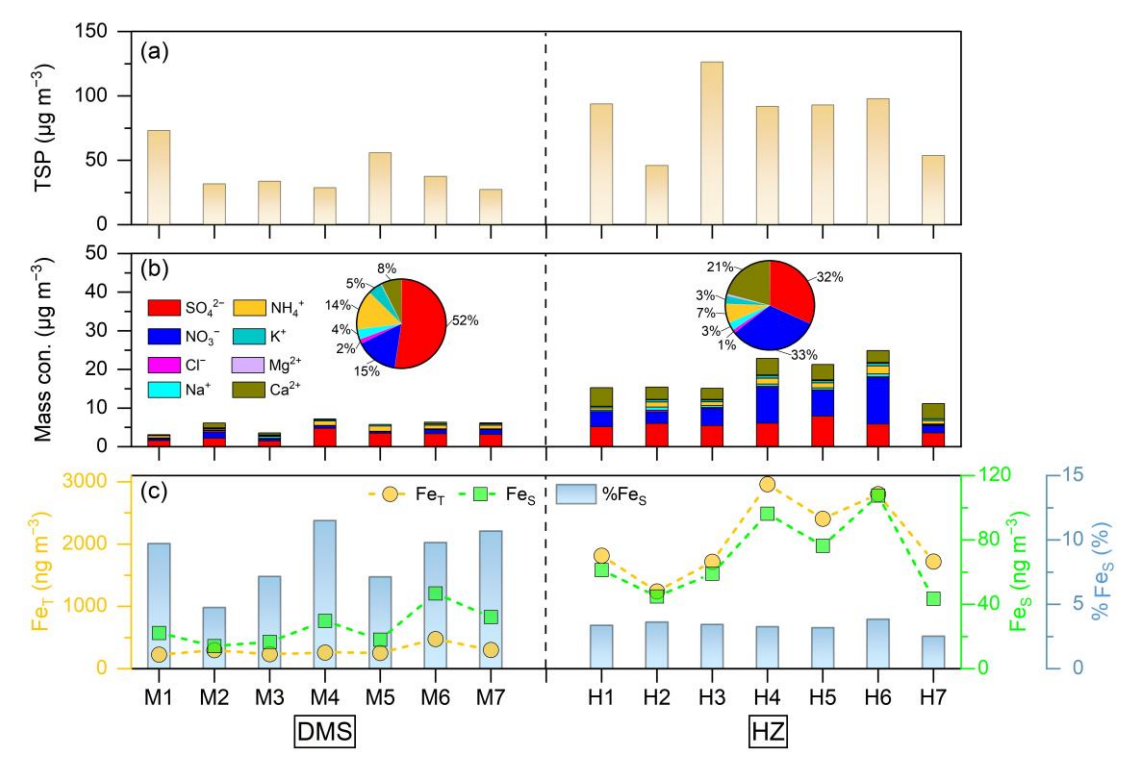


Figure 1: Time series of (a) total suspended particle (TSP), (b) chemical species, and (c) total Fe (Fe_T), soluble Fe (Fe_S) and Fe solubility (%Fe_S) in the mountain site (DMS) and the megacity of Hangzhou (HZ), respectively. The labels in X-axis denote the sample number series (M1-M7 and H1-H7) of TSP at DMS and in HZ, respectively.



180

185



3.2 Size distributions of major chemical species and Fe

Figure 2 illustrates the size distributions of SO_4^{2-} , NO_3^- , NH_4^+ , and Ca^{2+} , Fe_T , Fe_S , and %Fe_S in the sized-resolved aerosols. Since there were no MOUDI samples available in Hangzhou, we solely used MOUDI samples collected at the mountain site as an example. We observed significant differences in the size distributions of major ions. The results showed that SO_4^{2-} and NH_4^+ both peaked at the 0.56–1.0 µm size bin (Figures 2a–2b). In contrast, NO_3^- and Ca^{2+} peaked at 3.2–5.6 µm or 10–18 µm size bins (Figures 2c–2d), respectively. Sulfate accounted for more than 60% of the measured inorganic ions in the submicron particles ($D_p < 1$ µm) at the mountain site, whereas nitrate contributed only 5% (Figure S3a), consistent with the high sulfate fraction observed in TSP at DMS (Figure 1b). In contrast, nitrate dominated in the supermicron mode ($D_p > 1$ µm), representing 39% of the total inorganic ions and exceeding the sulfate fraction (33%) (Figure S4b).

We further explored size distributions of Fe_T, Fe_S and %Fe_S in the upper mixing layer (Figures 2e–2f). The size distribution of Fe_T exhibited a bimodal pattern with a major peak at 3.2–5.6 μm size bin in the supermicron particles and a minor peak (0.56–1.0 μm) in the submicron particles (Figure 2e). The main peak aligns with the size distribution of NO₃⁻. In contrast, the size distributions of Fe_S and %Fe_S exhibit similar peaks (0.56–1.0 μm) to those of SO₄²⁻ and NH₄⁺ in the submicron fraction. The low %Fe_S in supermicron particles coincided with the size distributions of NO₃⁻ and Ca²⁺ (Figures 2c–2d). We further simulated aerosol particle pH using the ISORROPIA-II model. As shown in Figure S4, supermicron particles exhibited a higher pH (4.0 ± 1.9) compared to submicron particles (2.5 ± 0.2), indicating that submicron particles were more acidic and thus more conducive to Fe acid dissolution. The implications of acid processing on aerosol Fe will be discussed later.





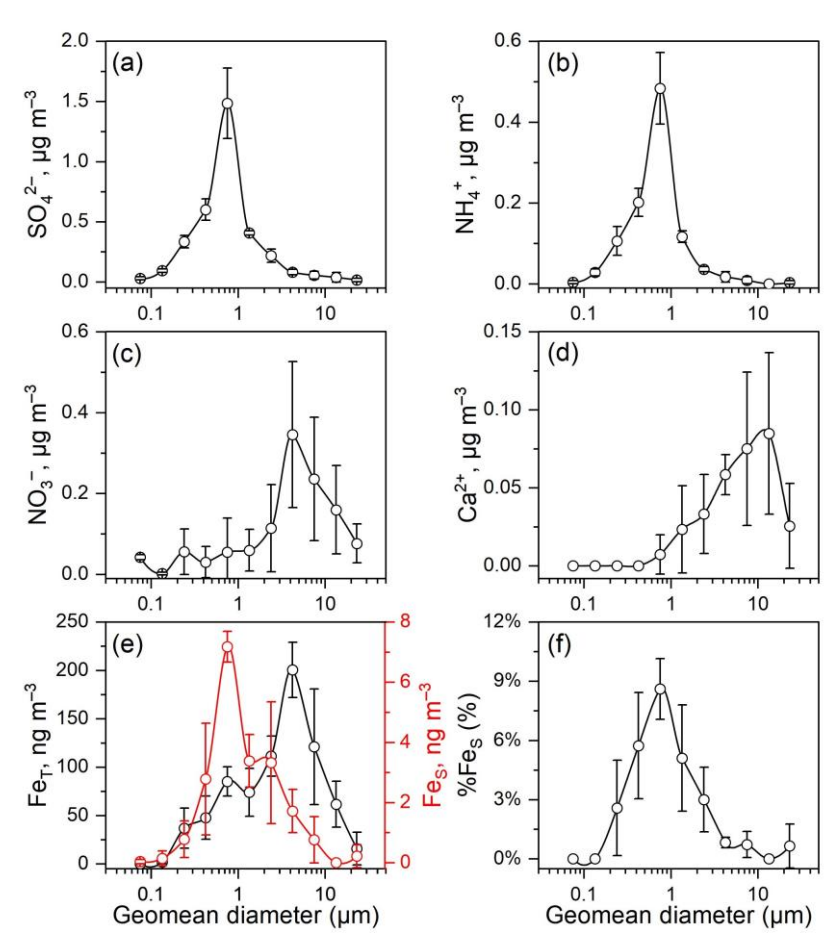


Figure 2: Size distributions of (a) SO_4^{2-} , (b) NH_4^+ , (c) NO_3^- , (d) Ca^{2+} , (e) Fe_T (black) and Fe_S (red), and (f) %Fe $_S$ in the size-resolved aerosols at the mountain site (DMS). The vertical bars represent one standard deviation for each diameter measurement.

3.3 Typical features of Fe dissolution

200

205

210

The ternary diagrams illustrate distinct features of %Fe_S and aerosol composition in two contrasting environments for TSP (Figure 3) and size-resolved aerosols (Figure 4, DMS only). As size-resolved aerosol samples were unavailable for Hangzhou, we simulated size-fractionated %Fe_S using the Integrated Massively Parallel Atmospheric Chemical Transport (IMPACT) model (Ito and Miyakawa, 2023; Ito et al., 2019; Ito and Xu, 2014). The model description and validation were presented in Figure S5 and Text S1 in the Supplement. Sulfate-rich particles cluster near the lower-right vertex, nitrate-rich particles near the top vertex, and ammonium- and calcium-rich particles near the left vertex of the ternary diagrams. In TSP, samples with high %Fe_S but low Fe_T predominantly occur near the sulfate vertex rather than the nitrate or ammonium-calcium apexes (Figure 3), suggesting that sulfuric acid dominates Fe dissolution in the upper mixing layer. In contrast, Hangzhou TSP samples (Figure 3) exhibit high Fe_T and low %Fe_S, positioned near the center or upper regions of the ternary



225



diagram. These points are scattered toward the nitrate and ammonium–calcium apexes and are characterized by a high proportion of nitrate and alkaline species (i.e., ammonium and calcium).

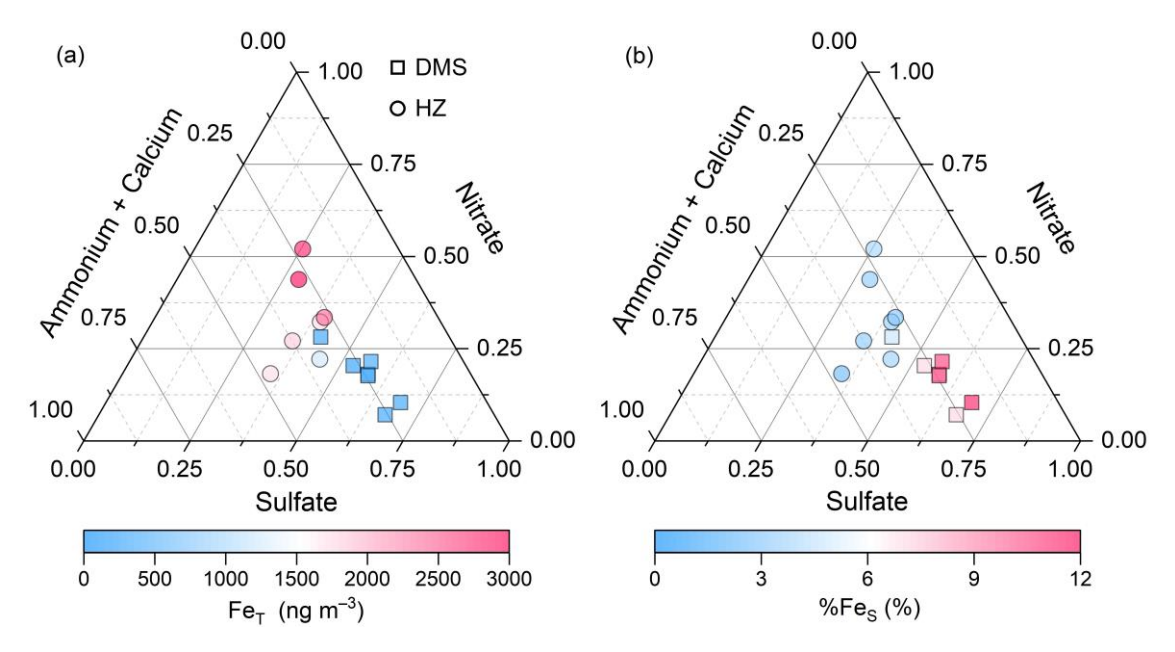


Figure 3: The ternary diagram of the relative abundances of sulfate, nitrate, and alkaline species (ammonium + calcium) in the total suspended particle (TSP) collected from the mountain site (DMS) and Hangzhou (HZ), respectively. The symbols (circles and squares) are colored by total Fe (Fe_T) in (a) and Fe solubility (%Fe_S) in (b).

In terms of %Fe_S in size-resolved aerosols, sulfate-rich particles are primarily distributed in the submicron mode in the upper mixing layer (Figure 4b), whereas nitrate-rich particles mainly occur in the supermicron range. In contrast, IMPACT simulations for %Fe_S in size-resolved aerosols in Hangzhou (Figure S6) show nitrate-rich particles concentrated in the submicron mode, differing from the upper-layer pattern. This is consistent with the higher nitrate contribution to TSP observed at the ground level in Hangzhou (Figure 1b).



235

240

245



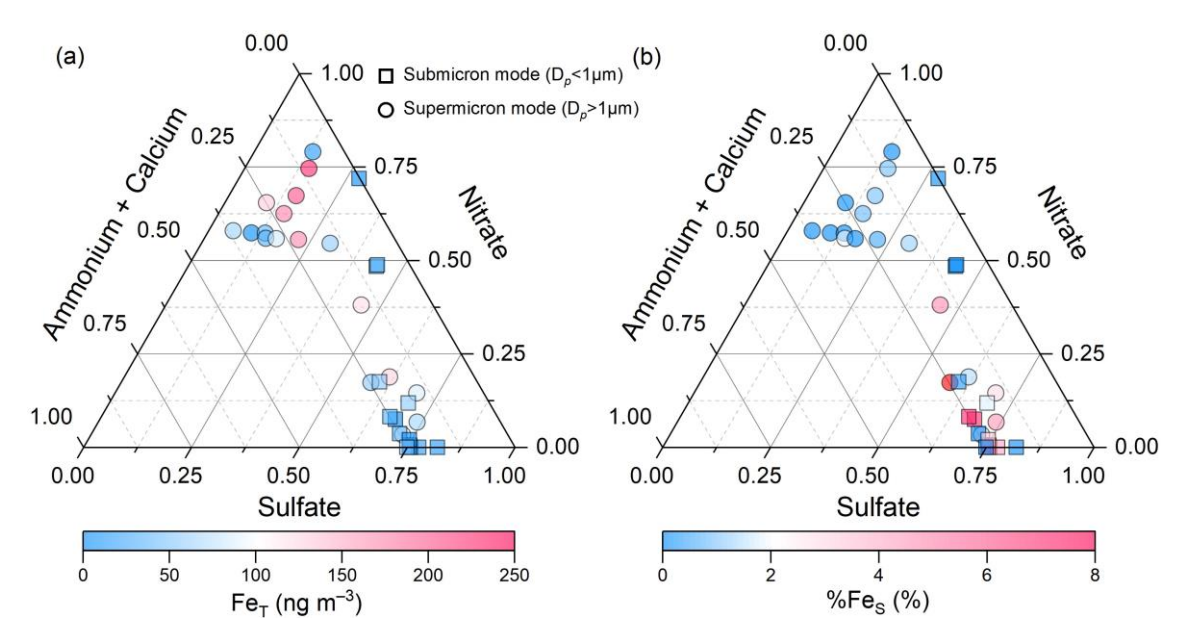


Figure 4: The ternary diagram of the relative abundances of sulfate, nitrate, and alkaline species (ammonium + calcium) in the size-resolved aerosols collected from the mountain site (DMS). The symbols (circles and squares) were colored by total Fe (Fe_T) in (a) and Fe solubility (%Fe_S) in (b).

Figure S7 shows the correlation matrix of aerosol compositions (SO₄²⁻, NO₃⁻, NH₄⁺ and Ca²⁺), Fe_T, Fe_S, %Fe_S, and aerosol pH in the size-resolved aerosols collected in the upper mixing layer (DMS). In the submicron particles, Fe_T and Fe_S displayed significant linear correlations with SO_4^{2-} , yielding positive correlation between SO_4^{2-} and %Fe_S (p < 0.01) (left bottom panel in Figure S7), which is consistent with previous studies (Oakes et al., 2012; Wong et al., 2020; Zhuang et al., 1992; Lei et al., 2023). Notably, no such correlations were found between NO₃⁻ and Fe_T, Fe_S, or %Fe_S in the submicron particles. This finding indicated that the sulfuric acid was the leading contributor to Fe dissolution in the submicron particles. However, the correlations of aerosol compositions, Fe_T, Fe_S, %Fe_S, and aerosol pH in the supermicron particles showed a contrasting pattern compared to the submicron particles (right panel in Figure S7). These relationships between SO₄²⁻ and Fe_S or %Fe_S were much weaker than those in the submicron particles. Moreover, SO₄²⁻ and Fe_T showed no significant correlation in the supermicron particles, whereas NO₃ was correlated well with Fe_T but not with Fe_S or %Fe_S. This is mainly due to the fact that total Fe is mainly derived from coarse particles such as mineral dust, as found in previous studies (Cwiertny et al., 2008; Longo et al., 2016; Meskhidze, 2005). Fe_s and %Fe_s in the supermicron particles exhibited significant negative correlations (p < 0.01 and p < 0.05) with aerosol pH. This may suggest that the Fe dissolution processing is sensitive to proton levels in the supermicron particles (Zhang et al., 2022; Chen et al., 2024b). It is also possible that there are fewer data points to reveal the relationship between Fe dissolution and aerosol acidity. Although a significant correlation was observed between NH₄⁺ and %Fe₅, this does not necessarily indicate that NH₄⁺ directly promotes Fe dissolution. As shown in Figure S7, NH₄+ exhibits a strong positive correlation with sulfate, but not with nitrate, in both submicron and





supermicron particles. This pattern likely reflects the association of ammonium with sulfate during acid processing, rather than a direct pH-buffering effect. The potential role of NH₄⁺ in Fe dissolution is further discussed in a later section.

4 Discussion

255

260

265

270

275

4.1 Distinct aging processes of acidic species at two heights

Previous studies have shown that the aging of acidic species influences both acid types and abundance in the atmosphere, thereby affecting Fe acidification (Hsu et al., 2010; Li et al., 2017; Srinivas et al., 2014). To delve deeper into the contribution of aging process of acidic species to Fe dissolution, the backward trajectories arriving at the upper mixing layer (DMS) and the ground-level (Hangzhou) and their corresponding molar ratios of sulfate to nitrate ($n[SO_4^{2-}]/n[NO_3^-]$) was investigated. As shown in Figure 5a, air masses reaching DMS primarily originated from the eastern ocean, passing through the megacities of Shanghai and Hangzhou. These trajectories traversed regions with relatively low NO_x emissions and arrived at DMS after long-range transport, resulting in elevated $n[SO_4^{2-}]/n[NO_3^-]$ ratios (5.4 ± 3.7), mostly exceeding 3. The increasing sulfate contribution with transport distance indicates significant aging of air pollutants during long-range transport (Longo et al., 2016; Itahashi et al., 2022; Chen et al., 2021). In contrast, air masses affecting Hangzhou mainly originated from the north, passing through nearby high-NO_x emission regions (Figure 5b). Their shorter transport paths correspond to a relatively brief atmospheric residence time, yielding lower $n[SO_4^{2-}]/n[NO_3^-]$ ratios (1.6 ± 0.7) and highlighting the dominant role of local emissions in nitric acid formation.

General, the significant differences in $n[SO_4^{2-}]/n[NO_3^-]$ ratios between the upper mixing layer and the ground-level indicate distinct aging processes. Compared to SO_2 , NO_x has a shorter residence time in the atmosphere, and it is more quickly oxidized to nitrate (Chen et al., 2021). Consequently, ratios of $n[SO_4^{2-}]/n[NO_3^-]$ tend to increase with the distance of long-range transport. This is explained by the long-range transport of air pollutants to DMS, where anthropogenic emissions are less or not anticipated. As shown in Figure S8, SO_2 column mass densities at both DMS and HZ were significantly lower than those in the urban areas to the northeast, suggesting that local emissions were not the primary contributors to sulfate levels at these locations. Backward trajectory analysis further revealed that air masses arriving at the upper mixing layer and Hangzhou had travelled over regions with elevated SO_2 levels prior to arrival, indicating that sulfate formation was largely driven by regional transport of upwind precursors. Additionally, as illustrated in Figure S9, the plume heights of air masses reaching the upper mixing layer and Hangzhou were predominantly below 1000 m, providing further evidence of aging process of particles intermingled with anthropogenic pollutants.





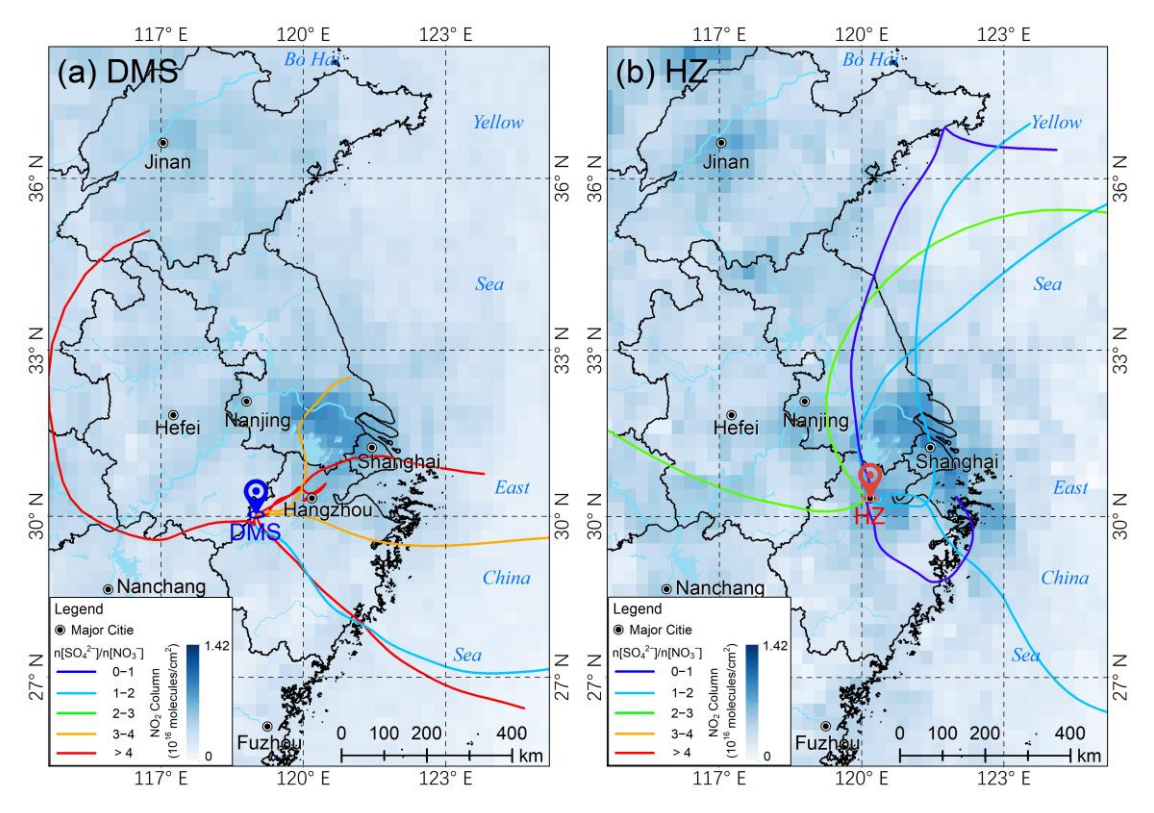


Figure 5: 48-h backward trajectories at 500 m a.g.l. (above ground level) and their corresponding $n[SO_4^{2-}]/n[NO_3^{-}]$ molar ratios during the sampling period. (a) Mountain (DMS), and (b) Hangzhou (HZ). Each trajectory represents a single sample, and it is derived from the NOAA HYSPLIT Trajectory Model (available at https://www.ready.noaa.gov/HYSPLIT_traj.php, accessed on September 3, 2024). The base map shows the spatial distribution of daily averaged tropospheric NO₂ column concentration with a spatial resolution of $0.25^{\circ} \times 0.25^{\circ}$ during the sampling periods. The data was obtained from Goddard Earth Sciences Data and Information Services Center (GES DISC) (available at https://giovanni.gsfc.nasa.gov/giovanni/, accessed on October 5, 2024).

4.2 Fe dissolution driven by acid processing

285

290

295

Although numerous studies have demonstrated that ligand-induced dissolution by organic acids can enhance %Fes (Deguillaume et al., 2005; Paris and Desboeufs, 2013), our results suggest that organic acids played a limited role in Fe dissolution (Figure S10 and Text S2 in the Supplement). Therefore, we focused primarily on the proton-promoted pathway. The molar ratio of acidic species (sulfate + nitrate) to total Fe is used as a proxy to qualitatively assess the impact of acrosol acidification on %Fes (Zhang et al., 2022; Shi et al., 2020; Liu et al., 2021; Zhu et al., 2022). Figure 6a shows that %Fes correlates strongly with $(n[SO_4^{2-}] + n[NO_3^{-}])/n[Fe_T]$ (p < 0.01), indicating that Fe dissolution is enhanced by acid processing. These ratios were higher at the mountain site than at Hangzhou, reflecting a greater degree of Fe acidification in the upper mixing layer and explaining the vertical differences in %Fes. Previous studies have shown that %Fes is higher under high relative humidity (RH) due to more efficient heterogeneous reactions on aqueous surfaces compared to dry particles (Shi et





al., 2020; Zhu et al., 2022). Indeed, we found that the RH was normally higher (88.1 \pm 5.8%) at DMS compared to RH at 70.5 \pm 9.3% in HZ. This suggests that the enhancement of aerosol water induced by high RH in the upper mixing layer provides an aqueous surface to foster Fe dissolution. Figure 7a presents Fe acidification process in the size-resolved aerosols. The results showed that the higher Fe acidification in submicron particles resulted in a relatively high %Fe_S (3.4 \pm 3.8%) in comparison to those in the supermicron particles (%Fe_S = 1.7 \pm 2.2%). This disparity aligns with the size-resolved aerosol acidity measurements, which showed that submicron particles exhibited lower pH (2.5 \pm 0.2) than supermicron particles (4.0 \pm 1.9). These results provide further evidence that stronger acid processing in submicron aerosols enhances Fe dissolution.

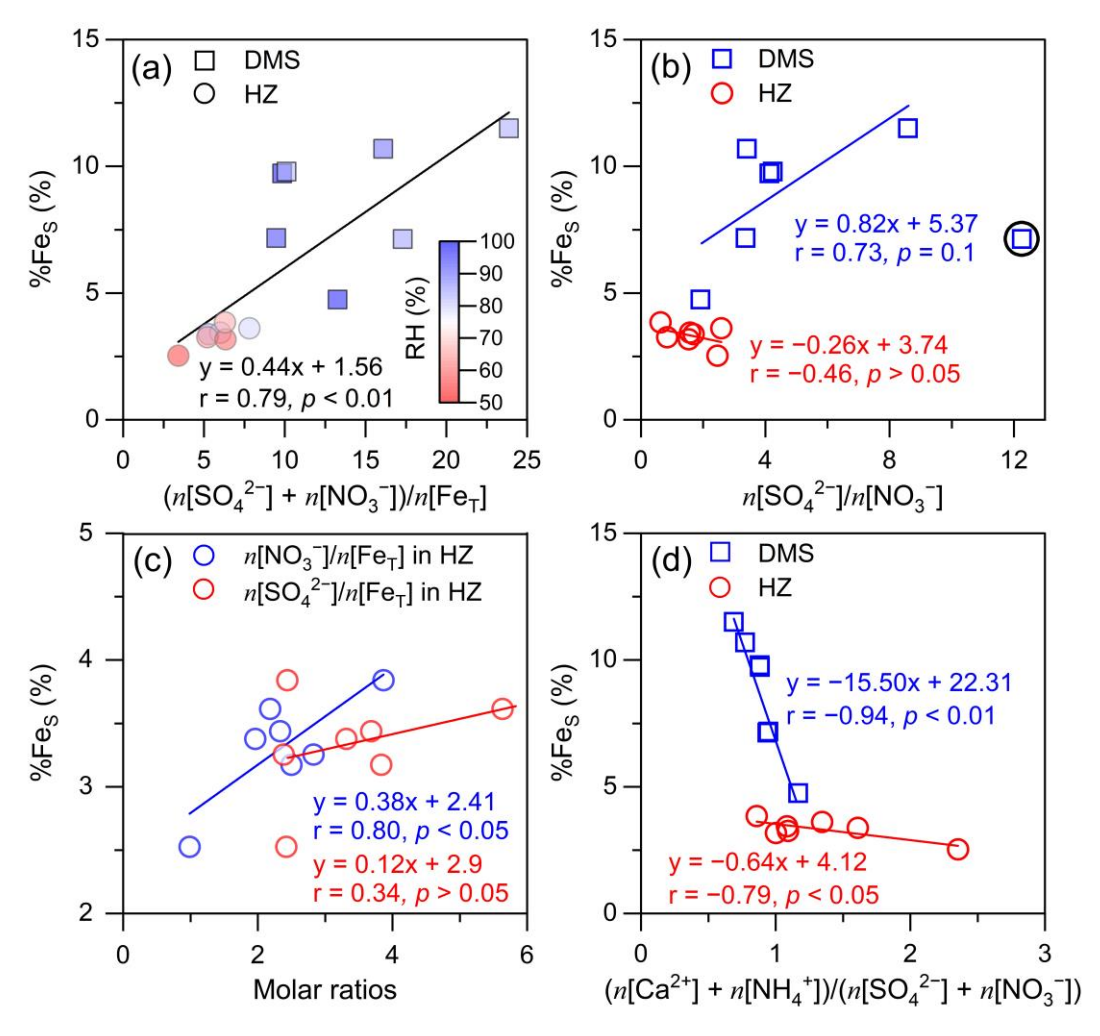


Figure 6: Correlations between %Fe_S and certain inorganic ions. (a) $(n[SO_4^{2-}] + n[NO_3^-])/n[Fe_T]$ versus %Fe_S, (b) $n[SO_4^{2-}] + n[NO_3^-]$ versus %Fe_S, (c) $n[SO_4^{2-}]$ or $n[NO_3^-]/n[Fe_T]$ versus %Fe_S in Hangzhou (HZ), and (d) $(n[Ca^{2+}] + n[NH_4^+])/(n[SO_4^{2-}] + n[NO_3^-])$ versus %Fe_S in TSP, respectively. Solid circles and squares are colored by relative humidity (RH) in (a). In plot b, one point is not included in the correlation analysis ascribed to relatively low NO₃⁻ and is indicated by the black circle.



315

320

325

330



4.3 Role of sulfuric acid versus nitric acid in Fe solubility

To identify contributions of the sulfuric acid and nitric acid to %Fe_S, we performed an in-depth analysis of the response of iron dissolution to acid processing driven by acidic species. The sulfate-to-nitrate molar ratio $(n[SO_4^2]/n[NO_3^-])$ serves as an indicator of the relative strength and dominance of inorganic acids. Figure 6b shows that %Fe_S exhibits a positive linear correlation with $n[SO_4^2]/n[NO_3^-]$ in the upper mixing layer but a weaker correlation in Hangzhou. This suggests that sulfuric acid plays a more important role in enhancing %Fe_S in the upper layer, consistent with the longer aging of air masses at high altitude (Section 4.1). Cwiertny et al. (2008) reported that an equivalent molar concentration of sulfuric acid dissolves ~32% more Fe from dust particles (Arizona Test Dust) than nitric acid. This might contribute to the differences we observed in our study between the sites but such an impact is not bigger enough to explain the large differences. To further quantify the contributions of the two acids in Hangzhou, we examined the molar ratios $n[NO_3^-]/n[Fe_T]$ and $n[SO_4^2^-]/n[Fe_T]$, following previous studies (Zhu et al., 2020; Hsu et al., 2014). The analysis revealed a significant correlation between $n[NO_3^-]/n[Fe_T]$ and %Fe_S was weak (r = 0.34, p > 0.05; Figure 6c). These results indicate that nitric acid likely dominates Fe acidification in urban aerosols, contrasting with the sulfuric acid-dominated Fe dissolution observed in the upper mixing layer.

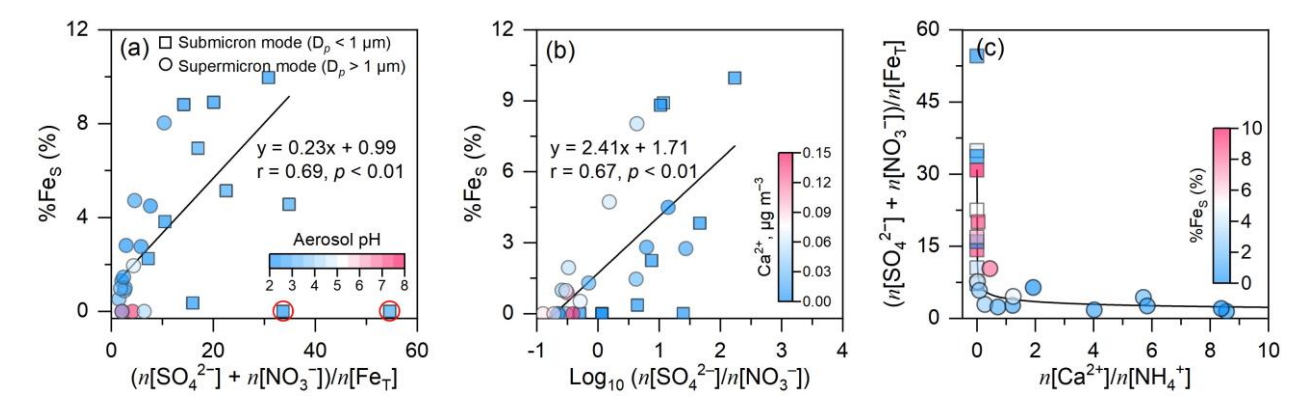


Figure 7: Scatter plots of (a) $(n[SO_4^{2-}] + n[NO_3^-])/n[Fe_T]$ versus %Fe_S, (b) $log_{10}(n[SO_4^{2-}] + n[NO_3^-])$ versus %Fe_S, and (c) $(n[Ca^{2+}]/n[NH_4^+])$ versus $(n[SO_4^{2-}] + n[NO_3^-])/n[Fe_T])$, respectively, in the size-resolved aerosols at DMS. Solid circles and squares are colored by aerosol pH, Ca^{2+} and %Fe_S in (a), (b), and (c), respectively. In plot a, two outliers are not included in the correlation analysis due to the relatively low Fe_T and are indicated by red circles.

Similar analysis revealed a significant positive correlation (p < 0.01) between %Fe_S and the $n[SO_4^{2-}]/n[NO_3^{-}]$ ratio across the size-resolved particles (Figure 7b). When $n[SO_4^{2-}]/n[NO_3^{-}]$ exceeded 1 ($log_{10}(n[SO_4^{2-}]/n[NO_3^{-}]) > 0$), high sulfate concentrations in submicron particles corresponded to the elevated %Fe_S. In contrast, when the ratio was below 1, %Fe_S in submicron particles was concentrated near the origin of the coordinate and did not exceed 3% (Figure 7b). This comparison



345



provides direct evidence that sulfuric acid plays a key role in enhancing Fe dissolution in the upper mixing layer, consistent with Section 4.2.

Here we noticed that high Ca^{2+} concentrations were primarily associated with NO_3^- levels and low %Fe_S in supermicron particles (Figure 7b), likely due to the buffering capacity of Ca^{2+} , which partially neutralizes aerosol acidity and inhibits Fe dissolution. To quantify this effect, the ratio of $(n[Ca^{2+}] + n[NH_4^+])$ to $(n[SO_4^{2-}] + n[NO_3^-])$ was used to represent the buffering capacity of alkaline species in TSP at both heights (Figure 6d). The results showed that %Fe_S was negatively correlated with $(n[Ca^{2+}] + n[NH_4^+])/(n[SO_4^{2-}] + n[NO_3^-])$ ratios at two heights, indicating that Fe dissolution is partially suppressed by the presence of alkaline species. The mean ratios were generally below 1 in the upper mixing layer (0.9 ± 0.1) and above 1 at the ground level (1.3 ± 0.5) , suggesting a weaker buffering effect aloft. Further analysis of the $n[Ca^{2+}]/n[NH_4^+]$ ratio identified the dominant alkaline species: buffering was primarily driven by NH_4^+ in submicron particles $(n[Ca^{2+}]/n[NH_4^+] < 1)$ and by Ca^{2+} in supermicron particles (Figure 7c).

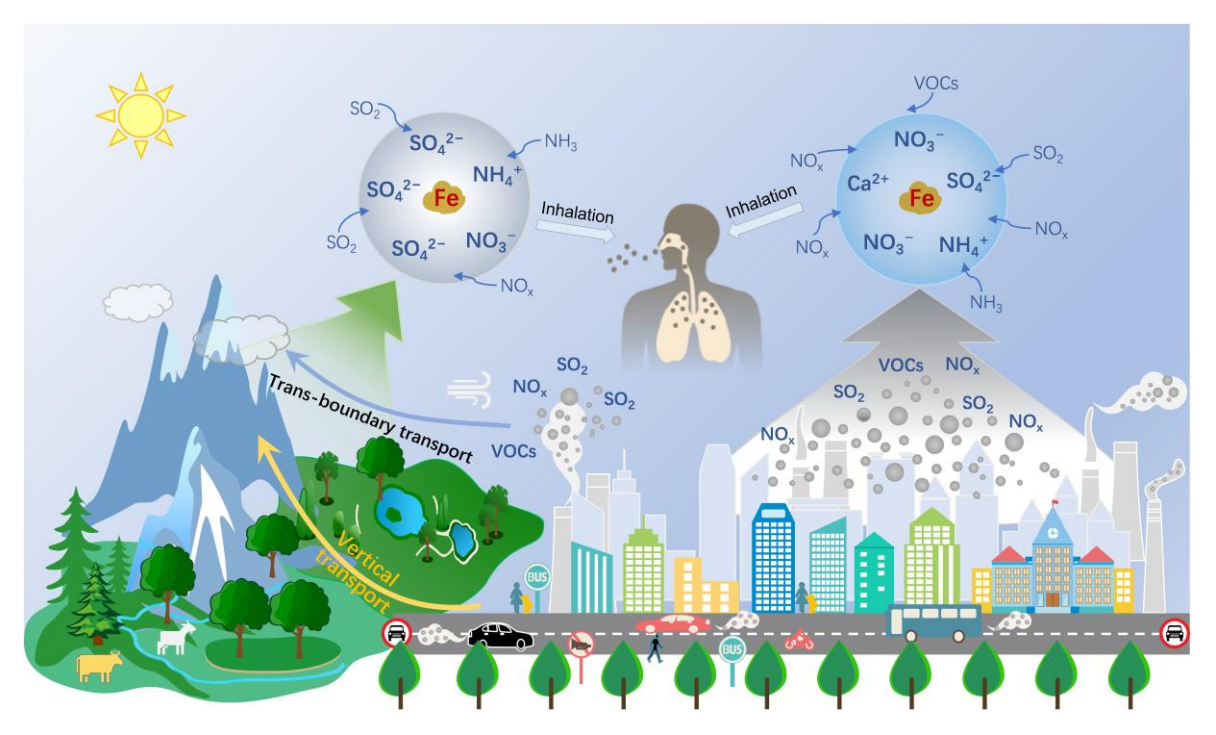


Figure 8: Schematic representation of the atmospheric iron acid dissolution in the upper mixing layer and at the ground-level and its potential implications for human health.

350 **5 Conclusions and Perspectives**

Our study elucidates significant vertical differences in the pathways in which Fe is dissolved by inorganic acids between the upper mixing layer and at the ground-level (Figure 8). The dissolution of Fe depends mainly on the process of



355

360

365

370

375

380



atmospheric acidification and the availability of acids in the atmosphere. The longer aging process, leading to more sulfuric vs nitric acid-dominates Fe dissolution in the upper mixing layer, in contrast to those in the urban environment. This difference leads to the distinct %Fe_S by acid processing in the two heights. Notably, nitric acid-driven Fe dissolution deserves more attention considering that NO_x has replaced SO₂ as the dominant chemical species in most parts of China and some cities around the world (Geng et al., 2024; Van Der A et al., 2017; Ooki and Uematsu, 2005). It's projected that the contribution of the elevated nitric acid to Fe dissolution tends to become important in megacities (Ooki and Uematsu, 2005).

While the distinct contribution of sulfuric and nitric acids to Fe dissolution in the upper mixing layer and at the ground-level is highlighted in this study, how this chemical pattern affects dissolved Fe concentration and deposition in numerical models has not been fully assessed by field observations (Liu et al., 2022; Ito, 2012). To better predict Fe dissolution and its impact on biogeochemical cycles, atmospheric chemistry models should place emphasis on the important contribution of nitric acid to Fe dissolution in the downwind locations (e.g., cities in the East Asia), where nitric acid replaces sulfuric acid as the dominant acidic species in the atmosphere (Itahashi et al., 2018; Uno et al., 2020). Our findings provide new data to test the ability of models to simulate these processes, helping to improve the accuracy of Fe concentration and dissolution predictions.

Our focus should pivot towards the health implications stemming from Fe acidification. Previous researches have revealed that the magnetite (Fe₃O₄) nanoparticles produced by combustion or friction-derived heating can enter the brain directly and in turn cause damage to the human brain (Maher et al., 2016; Kirschvink et al., 1992; Lu et al., 2020). Moreover, the Fe toxicity and its valence states (Fe(II) and Fe(III)) can generate ROS in aqueous reaction, causing oxidative stress and adverse health impacts (Chen et al., 2024a; Abbaspour et al., 2014; Song et al., 2024). As far as we know, to what extent airborne concentrations of iron nitrate affect human health is yet to be determined. Given that cities are the most densely populated and economically connected areas, traffic-related metal emissions are projected to increase. Future studies should pay more attention to the linkages between ambient nitrate, Fe dissolution, and potential adverse health impacts in urban regions (Figure 8).

Data availability. The data are available upon request to the corresponding author by email.

Author contributions. GCW and WJL conceived the study. GCW formulated the scientific questions, performed the data analysis, and wrote the manuscript. AI performed the model simulations. CW supported the measurement of NH₃. XDC, BYX, CW, MKZ, KLL, LX, QY, YTW, YLS, ZBS, AI, SXZ and WJL contributed to manuscript review and editing.

Competing interests. The authors declare no competing interests.





Acknowledgements. We acknowledge the Scientific Committee on Oceanic Research (SCOR) for their support of the Working Group 167, RUSTED (Reducing Uncertainty in Soluble aerosol Trace Element Deposition). We also acknowledge to Yue Wang for helping us with the sampling work.

Financial support. This work was financially supported by the National Natural Science Foundation of China (42277080; 42561160138), National Key Research and Development Program of China (2023YFC3706301), Postdoctoral Fellowship Program of CPSF (GZC20232275), State Key Laboratory of Atmospheric Boundary Layer Physics and Atmospheric Chemistry (LAPC-KF-2023-03), Joint Funds of the Zhejiang Provincial Natural Science Foundation of China (LZJMZ24D050009), and the MEXT-Program for the advanced studies of climate change projection (SENTAN) (JPMXD0722681344).

References

Abbaspour, N., Hurrell, R., and Kelishadi, R.: Review on iron and its importance for human health, Journal of Research in Medical Sciences, 19, 164–174, 2014.

Baker, A. R., Kanakidou, M., Nenes, A., Myriokefalitakis, S., Croot, P. L., Duce, R. A., Gao, Y., Guieu, C., Ito, A., Jickells,
T. D., Mahowald, N. M., Middag, R., Perron, M. M. G., Sarin, M. M., Shelley, R., and Turner, D. R.: Changing atmospheric acidity as a modulator of nutrient deposition and ocean biogeochemistry, Sci. Adv., 7, eabd8800,
https://doi.org10.1126/sciadv.abd8800, 2021.

Bougiatioti, A., Nikolaou, P., Stavroulas, I., Kouvarakis, G., Weber, R., Nenes, A., Kanakidou, M., and Mihalopoulos, N.: Particle water and pH in the eastern Mediterranean: source variability and implications for nutrient availability, Atmos.

400 Chem. Phys., 16, 4579–4591, https://doi.org10.5194/acp-16-4579-2016, 2016.

https://doi.org10.1016/j.atmosenv.2021.118255, 2021.

- Boyd, P. W. and Ellwood, M. J.: The biogeochemical cycle of iron in the ocean, Nat. Geosci., 3, 675–682, https://doi.org10.1038/ngeo964, 2010.
- Boyd, P. W., Jickells, T., Law, C. S., Blain, S., Boyle, E. A., Buesseler, K. O., Coale, K. H., Cullen, J. J., de Baar, H. J. W., Follows, M., Harvey, M., Lancelot, C., Levasseur, M., Owens, N. P. J., Pollard, R., Rivkin, R. B., Sarmiento, J., Schoemann,
- V., Smetacek, V., Takeda, S., Tsuda, A., Turner, S., and Watson, A. J.: Mesoscale Iron Enrichment Experiments 1993-2005:
 Synthesis and Future Directions, Science, 315, 612–617, https://doi.org10.1126/science.1131669, 2007.
 Chen, C., Tan, H., Hong, Y., Yin, C., Deng, X., Chan, P., Wu, M., Bu, Q., Weng, J., and Gan, Q.: Characteristics, formation mechanisms, and sources of non-refractory submicron aerosols in Guangzhou, China, Atmos. Environ., 250, 118255,
- Chen, H., Laskin, A., Baltrusaitis, J., Gorski, C. A., Scherer, M. M., and Grassian, V. H.: Coal fly ash as a source of iron in atmospheric dust, Environ. Sci. Technol., 46, 2112–2120, https://doi.org10.1021/es204102f, 2012.





- Chen, X., Wu, D., Zheng, L., Chen, Y., Cheng, A., and Li, Q.: Variable Valence State of Trace Elements Regulating Toxic Potencies of Inorganic Particulate Matter, Environ. Sci. Technol. Lett., 11, 223–229, https://doi.org10.1021/acs.estlett.4c00019, 2024a.
- Chen, Y., Wang, Z., Fang, Z., Huang, C., Xu, H., Zhang, H., Zhang, T., Wang, F., Luo, L., Shi, G., Wang, X., and Tang, M.: Dominant Contribution of Non-dust Primary Emissions and Secondary Processes to Dissolved Aerosol Iron, Environ. Sci. Technol., 58, 17355–17363, https://doi.org10.1021/acs.est.4c05816, 2024b.
 Cwiertny, D. M., Baltrusaitis, J., Hunter, G. J., Laskin, A., Scherer, M. M., and Grassian, V. H.: Characterization and acid-mobilization study of iron-containing mineral dust source materials, J. Geophys. Res.: Atmos., 113, D05202,
- https://doi.org10.1029/2007jd009332, 2008.
 Deguillaume, L., Leriche, M., Desboeufs, K., Mailhot, G., George, C., and Chaumerliac, N.: Transition Metals in Atmospheric Liquid Phases-Sources, Reactivity, and Sensitive Parameters, Chem. Rev., 105, 3388–3431, 2005.
 Fang, T., Guo, H., Zeng, L., Verma, V., Nenes, A., and Weber, R. J.: Highly Acidic Ambient Particles, Soluble Metals, and Oxidative Potential: A Link between Sulfate and Aerosol Toxicity, Environ. Sci. Technol., 51, 2611–2620,
- https://doi.org10.1021/acs.est.6b06151, 2017.

 Fountoukis, C. and Nenes, A.: ISORROPIA II: a computationally efficient thermodynamic equilibrium model for K⁺–Ca²⁺– Mg²⁺–NH₄⁺ –Na⁺–SO₄²⁻ –NO₃⁻ –Cl⁻–H₂O aerosols, Atmos. Chem. Phys., 7, 4639–4659, 2007.

 Geng, G., Liu, Y., Liu, Y., Liu, S., Cheng, J., Yan, L., Wu, N., Hu, H., Tong, D., Zheng, B., Yin, Z., He, K., and Zhang, Q.: Efficacy of China's clean air actions to tackle PM_{2.5} pollution between 2013 and 2020, Nat. Geosci., 17, 987–994,
- 430 https://doi.org10.1038/s41561-024-01540-z, 2024.
 - Hangzhou Overview-Population and Employment:
 - https://eng.hangzhou.gov.cn/art/2024/6/17/art_1229498044_58876294.html, last access: 2024-06-17.
 - Hsu, S. C., Gong, G. C., Shiah, F. K., Hung, C. C., Kao, S. J., Zhang, R., Chen, W. N., Chen, C. C., Chou, C. C. K., Lin, Y. C., Lin, F. J., and Lin, S. H.: Sources, solubility, and acid processing of aerosol iron and phosphorous over the South China
- Sea: East Asian dust and pollution outflows vs. Southeast Asian biomass burning, Atmos. Chem. Phys. Discuss., 14, 21433–21472, https://doi.org10.5194/acpd-14-21433-2014, 2014.
 - Hsu, S. C., Liu, S. C., Arimoto, R., Shiah, F. K., Gong, G. C., Huang, Y. T., Kao, S. J., Chen, J. P., Lin, F. J., Lin, C. Y., Huang, J. C., Tsai, F., and Lung, S. C. C.: Effects of acidic processing, transport history, and dust and sea salt loadings on the dissolution of iron from Asian dust, J. Geophys. Res.: Atmos., 115, D19313, https://doi.org10.1029/2009jd013442, 2010.
- Ingall, E. D., Feng, Y., Longo, A. F., Lai, B., Shelley, R. U., Landing, W. M., Morton, P. L., Violaki, K., Gao, Y., Sahai, S., and Castorina, E.: Enhanced Iron Solubility at Low pH in Global Aerosols, Atmosphere, 9, 201, https://doi.org10.3390/atmos9050201, 2018.
 - Itahashi, S., Hattori, S., Ito, A., Sadanaga, Y., Yoshida, N., and Matsuki, A.: Role of Dust and Iron Solubility in Sulfate Formation during the Long-Range Transport in East Asia Evidenced by ¹⁷O-Excess Signatures, Environ. Sci. Technol., 56,
- 445 13634–13643, https://doi.org10.1021/acs.est.2c03574, 2022.





- Itahashi, S., Yumimoto, K., Uno, I., Hayami, H., Fujita, S.-i., Pan, Y., and Wang, Y.: A 15-year record (2001–2015) of the ratio of nitrate to non-sea-salt sulfate in precipitation over East Asia, Atmos. Chem. Phys., 18, 2835-2852, https://doi.org10.5194/acp-18-2835-2018, 2018.
- Ito, A.: Contrasting the Effect of Iron Mobilization on Soluble Iron Deposition to the Ocean in the Northern and Southern

 450 Hemispheres, Journal of the Meteorological Society of Japan. Ser. II, 90A, 167–188, https://doi.org10.2151/jmsj.2012-A09,
 2012.
 - Ito, A. and Miyakawa, T.: Aerosol Iron from Metal Production as a Secondary Source of Bioaccessible Iron, Environ. Sci. Technol., 57, 4091–4100, https://doi.org10.1021/acs.est.2c06472, 2023.
 - Ito, A. and Shi, Z.: Delivery of anthropogenic bioavailable iron from mineral dust and combustion aerosols to the ocean,
- 455 Atmos. Chem. Phys., 16, 85–99, https://doi.org10.5194/acp-16-85-2016, 2016.
 - Ito, A. and Xu, L.: Response of acid mobilization of iron-containing mineral dust to improvement of air quality projected in the future, Atmos. Chem. Phys., 14, 3441–3459, https://doi.org10.5194/acp-14-3441-2014, 2014.
 - Ito, A., Myriokefalitakis, S., Kanakidou, M., Mahowald, N. M., Scanza, R. A., Hamilton, D. S., Baker, A. R., Jickells, T., Sarin, M., Bikkina, S., Gao, Y., Shelley, R. U., Buck, C. S., Landing, W. M., Bowie, A. R., Perron, M. M. G., Guieu, C.,
- Meskhidze, N., Johnson, M. S., Feng, Y., Kok, J. F., Nenes, A., and A., D. R.: Pyrogenic iron: The missing link to high iron solubility in aerosols, Sci. Adv., 5, eaau7671, https://doi.org10.1126/sciadv.aau7671, 2019.
 - Jickells, T. D., An, Z. S., Andersen, K. K., Baker, A. R., Bergametti, G., Brooks, N., Cao, J. J., Boyd, P. W., Duce, R. A., Hunter, K. A., Kawahata, H., Kubilay, N., laRoche, J., Liss, P. S., Mahowald, N., Prospero, J. M., Ridgwell, A. J., Tegen, I., and Torres, R.: Global Iron Connections Between Desert Dust, Ocean Biogeochemistry, and Climate, Science, 308, 67–71,
- 465 https://doi.org10.1126/science.1105959, 2005.
 - Kirschvink, J. L., Kobayashi-Kirschvink, A., and Woodford, B. J.: Magnetite biomineralization in the human brain, Proc. Natl. Acad. Sci., 89, 7683–7687, https://doi.org10.1073/pnas.89.16.768, 1992.
 - Kunwar, B. and Kawamura, K.: One-year observations of carbonaceous and nitrogenous components and major ions in the aerosols from subtropical Okinawa Island, an outflow region of Asian dusts, Atmos. Chem. Phys., 14, 1819–1836,
- 470 https://doi.org10.5194/acp-14-1819-2014, 2014.
 - Lei, Y., Li, D., Lu, D., Zhang, T., Sun, J., Wang, X., Xu, H., and Shen, Z.: Insights into the roles of aerosol soluble iron in secondary aerosol formation, Atmos. Environ., 294, 119507, https://doi.org10.1016/j.atmosenv.2022.119507, 2023. Li, W. J., Xu, L., Liu, X. H., Zhang, J. C., Lin, Y. T., Yao, X. H., Gao, H. W., Zhang, D. Z., Chen, J. M., Wang, W. X.,
 - Harrison, R. M., Zhang, X. Y., Shao, L. Y., Fu, P. Q., Nenes, A., and Shi, Z. B.: Air pollution-aerosol interactions produce
- more bioavailable iron for ocean ecosystems, Sci. Adv., 3, e1601749, https://doi.org10.1126/sciadv.1601749, 2017. Liu, L., Lin, Q., Liang, Z., Du, R., Zhang, G., Zhu, Y., Qi, B., Zhou, S., and Li, W.: Variations in concentration and solubility of iron in atmospheric fine particles during the COVID-19 pandemic: An example from China, Gondwana Res., 97, 138–144, https://doi.org10.1016/j.gr.2021.05.022, 2021.



495



- Liu, M. X., Matsui, H., Hamilton, D. S., and Lamb, K. D.: The underappreciated role of anthropogenic sources in atmospheric soluble iron flux to the Southern Ocean, npj Clim. Atmos. Sci., 5, 28, https://doi.org10.1038/s41612-022-00250-w, 2022.
 - Longo, A. F., Feng, Y., Lai, B., Landing, W. M., Shelley, R. U., Nenes, A., Mihalopoulos, N., Violaki, K., and Ingall, E. D.: Influence of Atmospheric Processes on the Solubility and Composition of Iron in Saharan Dust, Environ. Sci. Technol., 50, 6912–6920, https://doi.org10.1021/acs.est.6b02605, 2016.
- Lu, D., Luo, Q., Chen, R., Zhuansun, Y., Jiang, J., Wang, W., Yang, X., Zhang, L., Liu, X., Li, F., Liu, Q., and Jiang, G.: Chemical multi-fingerprinting of exogenous ultrafine particles in human serum and pleural effusion, Nat. Commun., 11, 2567, https://doi.org10.1038/s41467-020-16427-x, 2020.
 - Maher, B. A., Ahmed, I. A., Karloukovski, V., MacLaren, D. A., Foulds, P. G., Allsop, D., Mann, D. M., Torres-Jardon, R., and Calderon-Garciduenas, L.: Magnetite pollution nanoparticles in the human brain, Proc. Natl. Acad. Sci., 113,
- 10797–10801, https://doi.org10.1073/pnas.1605941113, 2016.
 Mahowald, N. M., Engelstaedter, S., Luo, C., Sealy, A., Artaxo, P., Benitez-Nelson, C., Bonnet, S., Chen, Y., Chuang, P. Y., Cohen, D. D., Dulac, F., Herut, B., Johansen, A. M., Kubilay, N., Losno, R., Maenhaut, W., Paytan, A., Prospero, J. M., Shank, L. M., and Siefert, R. L.: Atmospheric Iron Deposition: Global Distribution, Variability, and Human Perturbations,
 - Annu. Rev. Mar. Science, 1, 245–278, https://doi.org10.1146/annurev.marine.010908.163727, 2009. Martin, J. H.: Glacial-interglacial CO₂ change: The Iron Hypothesis, Paleoceanography, 5, 1–13,
 - Martínez-García, A., Sigman, D. M., Ren, H. J., Anderson, R. F., Straub, M., Hodell, D. A., Jaccard, S. L., Eglinton, T. I., and Haug, G. H.: Iron Fertilization of the Subantarctic Ocean During the Last Ice Age, Science, 343, 1347–1350, https://doi.org10.1126/science.1246, 2014.
- Meskhidze, N.: Iron mobilization in mineral dust: Can anthropogenic SO₂ emissions affect ocean productivity?, Geophys. Res. Lett., 30, 2085, https://doi.org10.1029/2003gl018035, 2003.
 - Meskhidze, N.: Dust and pollution: A recipe for enhanced ocean fertilization?, J. Geophys. Res., 110, D03301, https://doi.org10.1029/2004jd005082, 2005.
- Oakes, M., Rastogi, N., Majestic, B. J., Shafer, M., Schauer, J. J., Edgerton, E. S., and Weber, R. J.: Characterization of soluble iron in urban aerosols using near real time data, J. Geophys. Res.: Atmos., 115, D15302,
 - https://doi.org10.1029/2009jd012532, 2010.

https://doi.org10.1029/PA005i001p00001, 1990.

- Oakes, M., Ingall, E. D., Lai, B., Shafer, M. M., Hays, M. D., Liu, Z. G., Russell, A. G., and Weber, R. J.: Iron Solubility Related to Particle Sulfur Content in Source Emission and Ambient Fine Particles, Environ. Sci. Technol., 46, 6637–6644, https://doi.org10.1021/es300701c, 2012.
- Ooki, A. and Uematsu, M.: Chemical interactions between mineral dust particles and acid gases during Asian dust events, J. Geophys. Res.: Atmos., 110, D03201, https://doi.org10.1029/2004jd004737, 2005.



520

540



- Paris, R. and Desboeufs, K. V.: Effect of atmospheric organic complexation on iron-bearing dust solubility, Atmos. Chem. Phys., 13, 4895–4905, https://doi.org10.5194/acp-13-4895-2013, 2013.
- Rubasinghege, G., Lentz, R. W., Scherer, M. M., and Grassian, V. H.: Simulated atmospheric processing of iron oxyhydroxide minerals at low pH: roles of particle size and acid anion in iron dissolution, Proc. Natl. Acad. Sci., 107, 6628-6633, https://doi.org10.1073/pnas.0910809107, 2010.
 - Sakata, K., Sakaguchi, A., Yamakawa, Y., Miyamoto, C., Kurisu, M., and Takahashi, Y.: Measurement report: Stoichiometry of dissolved iron and aluminum as an indicator of the factors controlling the fractional solubility of aerosol iron: Results of the annual observations of size-fractionated aerosol particles in Japan, Atmos. Chem. Phys., 23, 9815–9836,
- https://doi.org10.5194/acp-23-9815-2023, 2023. Shi, J., Guan, Y., Ito, A., Gao, H., Yao, X., Baker, A. R., and Zhang, D.: High Production of Soluble Iron Promoted by Aerosol Acidification in Fog, Geophys. Res. Lett., 47, e2019GL086124, https://doi.org10.1029/2019gl086124, 2020. Shi, Z., Krom, M. D., Bonneville, S., and Benning, L. G.: Atmospheric processing outside clouds increases soluble iron in mineral dust, Environ. Sci. Technol., 49, 1472-1477, https://doi.org10.1021/es504623x, 2015.
- 525 Song, X., Wu, D., Chen, X., Ma, Z., Li, Q., and Chen, J.: Toxic Potencies of Particulate Matter from Typical Industrial Plants Mediated with Acidity via Metal Dissolution, Environ. Sci. Technol., 58, 6736-6743, https://doi.org10.1021/acs.est.4c00929, 2024.
 - Srinivas, B., Sarin, M. M., and Kumar, A.: Impact of anthropogenic sources on aerosol iron solubility over the Bay of Bengal and the Arabian Sea, Biogeochemistry, 110, 257-268, https://doi.org10.1007/s10533-011-9680-1, 2011.
- 530 Srinivas, B., Sarin, M. M., and Rengarajan, R.: Atmospheric transport of mineral dust from the Indo - Gangetic Plain: Temporal variability, acid processing, and iron solubility, Geochem. Geophys. Geosyst., 15, 3226–3243, https://doi.org10.1002/2014GC005395, 2014.
 - Uno, I., Wang, Z., Itahashi, S., Yumimoto, K., Yamamura, Y., Yoshino, A., Takami, A., Hayasaki, M., and Kim, B. G.: Paradigm shift in aerosol chemical composition over regions downwind of China, Sci. Rep., 10, 6450,
- https://doi.org10.1038/s41598-020-63592-6, 2020. 535
 - van der A, R. J., Mijling, B., Ding, J., Koukouli, M. E., Liu, F., Li, Q., Mao, H., and Theys, N.: Cleaning up the air: effectiveness of air quality policy for SO₂ and NO_x emissions in China, Atmos. Chem. Phys., 17, 1775–1789, https://doi.org10.5194/acp-17-1775-2017, 2017.
 - Vidrio, E., Jung, H., and Anastasio, C.: Generation of Hydroxyl Radicals from Dissolved Transition Metals in Surrogate
- Lung Fluid Solutions, Atmos. Environ., 42, 4369–4379, https://doi.org10.1016/j.atmosenv.2008.01.004, 2008. Wang, G. C., Chen, J., Xu, J., Yun, L., Zhang, M. D., Li, H., Qin, X. F., Deng, C. R., Zheng, H. T., Gui, H. Q., Liu, J. G., and Huang, K.: Atmospheric Processing at the Sea-Land Interface Over the South China Sea: Secondary Aerosol Formation, Aerosol Acidity, and Role of Sea Salts, J. Geophys. Res.: Atmos., 127, e2021JD036255, https://doi.org10.1029/2021JD036255, 2022.





- Wang, Z., Wang, T., Fu, H., Zhang, L., Tang, M., George, C., Grassian, V. H., and Chen, J.: Enhanced heterogeneous uptake of sulfur dioxide on mineral particles through modification of iron speciation during simulated cloud processing, Atmos. Chem. Phys., 19, 12569–12585, https://doi.org10.5194/acp-19-12569-2019, 2019.
 - Wong, J. P. S., Yang, Y., Fang, T., Mulholland, J. A., Russell, A. G., Ebelt, S., Nenes, A., and Weber, R. J.: Fine Particle Iron in Soils and Road Dust Is Modulated by Coal-Fired Power Plant Sulfur, Environ. Sci. Technol., 54, 7088–7096,
- 550 <u>https://doi.org10.1021/acs.est.0c00483</u>, 2020.
 - Xu, L., Zhi, M., Liu, X., Gao, H., Yao, X., Yuan, Q., Fu, P., and Li, W.: Direct evidence of pyrogenic aerosol iron by intrusions of continental polluted air into the Eastern China Seas, Atmos. Res., 292, 106839, https://doi.org10.1016/j.atmosres.2023.106839, 2023.
 - Zhang, H., Li, R., Dong, S., Wang, F., Zhu, Y., Meng, H., Huang, C., Ren, Y., Wang, X., Hu, X., Li, T., Peng, C., Zhang, G.,
- Xue, L., Wang, X., and Tang, M.: Abundance and Fractional Solubility of Aerosol Iron During Winter at a Coastal City in Northern China: Similarities and Contrasts Between Fine and Coarse Particles, J. Geophys. Res.: Atmos., 127, e2021JD036070, https://doi.org10.1029/2021jd036070, 2022.
 - Zheng, B., Tong, D., Li, M., Liu, F., Hong, C., Geng, G., Li, H., Li, X., Peng, L., Qi, J., Yan, L., Zhang, Y., Zhao, H., Zheng, Y., He, K., and Zhang, Q.: Trends in China's anthropogenic emissions since 2010 as the consequence of clean air actions,
- 560 Atmos. Chem. Phys., 18, 14095–14111, https://doi.org10.5194/acp-18-14095-2018, 2018.
 - Zhi, M., Wang, G., Xu, L., Li, K., Nie, W., Niu, H., Shao, L., Liu, Z., Yi, Z., Wang, Y., Shi, Z., Ito, A., Zhai, S., and Li, W.: How Acid Iron Dissolution in Aged Dust Particles Responds to the Buffering Capacity of Carbonate Minerals during Asian Dust Storms, Environ. Sci. Technol., 59, 6167–6178, https://doi.org10.1021/acs.est.4c12370, 2025.
 - Zhu, X. R., Prospero, J. M., and Millero, F. J.: Diel variability of soluble Fe(II) and soluble total Fe in North African dust in
- the trade winds at Barbados, J. Geophys. Res.: Atmos., 102, 21297–21305, https://doi.org10.1029/97jd01313, 1997. Zhu, Y., Li, W., Wang, Y., Zhang, J., Liu, L., Xu, L., Xu, J., Shi, J., Shao, L., Fu, P., Zhang, D., and Shi, Z.: Sources and processes of iron aerosols in a megacity in Eastern China, Atmos. Chem. Phys., 22, 2191–2202, https://doi.org10.5194/acp-22-2191-2022, 2022.
 - Zhu, Y. H., Li, W. J., Lin, Q. H., Yuan, Q., Liu, L., Zhang, J., Zhang, Y. X., Shao, L. Y., Niu, H. Y., Yang, S. S., and Shi, Z.
- B.: Iron solubility in fine particles associated with secondary acidic aerosols in east China, Environ. Pollut., 264, 114769, https://doi.org10.1016/j.envpol.2020.114769, 2020.
 - Zhuang, G. S., Yi, Z., Duce, R. A., and Brown, P. R.: Link between iron and sulphur cycles suggested by detection of Fe(II) in remote marine aerosols, Nature, 355, 537–539, 1992.